Research Article | Vol. 29, No. 20 / 27 Sep 2021 / Optics Express 32051
Optics EXPRESS

Ultrafast laser-induced strain waves in thin ruthenium layers

G. DE HAAN,[1,2,*] T. J. VAN DEN HOOVEN,[1,2] AND P. C. M. PLANKEN[1,2]

[1]*Advanced Research Center for Nanolithography (ARCNL), Science Park 106, 1098 XG Amsterdam, The Netherlands*
[2]*Van der Waals-Zeeman Institute, University of Amsterdam, Science Park 904, 1098 XH Amsterdam, The Netherlands*
[*]*g.dehaan@arcnl.nl*

Abstract: We report on the time-dependent optical diffraction from ultra-high frequency laser-induced acoustic waves in thin layers of ruthenium deposited on glass substrates. We show that the thermo-optic and strain-optic effects dominate the optical response of Ru layers to a traveling longitudinal strain wave. In addition, we show the generation and detection of acoustic waves with a central frequency ranging from 130 GHz to 750 GHz on ultra-thin layers with thicknesses in the range of 1.2 - 20 nm. For these ultra-thin layers we measure a strong dependency of the speed of sound on the layer thickness and, thus, the frequency. This frequency-dependent speed of sound results in a frequency-dependent acoustic impedance mismatch between the ruthenium and the glass substrate, leading to a faster decay of the measured signals for increasing frequency. Furthermore, for these extremely high-frequency oscillations, we find that the frequency and phase remain constant for times longer than about 2 ps after optical excitation. Back extrapolation of the acquired acoustic signals to t = 0 gives a starting phase of $-\pi/2$. As this seems unlikely, we interpret this as an indication of possible dynamic changes in the phase/frequency of the acoustic wave in the first 2 ps after excitation.

1. Introduction

The study of thin films with ultra-fast laser-induced acoustic waves has seen a lot of development in the past decades. Major advancements in the fundamental understanding of photo-acoustics have been made with regards to the generation, propagation, and detection of high-frequency acoustic waves [1–3]. The ability of acoustic waves to travel through optically opaque materials has many applications, such as detection of buried structures [4–7] and photo-acoustic imaging [8,9]. Furthermore, laser-induced acoustic waves have been used to access and investigate a multitude of material properties and physical phenomena [10–27].

A less well-known candidate for photo-acoustic studies is ruthenium (Ru). Ru has a relatively high electron-phonon coupling constant of 1.85×10^{18} $\mathrm{Wm^{-3}K^{-1}}$, a relatively small optical penetration depth of about 6 nm at a wavelength of 400 nm, and a relatively modest electronic thermal conductivity of 117 $\mathrm{Wm^{-1}K^{-1}}$ compared to other metals commonly used in photo-acoustic studies, such as gold and silver [28,29]. In addition, Ru has a high melting point of 2583 K. When an ultra-short laser pulse is used to illuminate a Ru layer, these parameters suggest that significant amounts of energy can be deposited in a thin layer near the surface, leading to the generation of extremely high-frequency longitudinal strain waves. Furthermore, thin layers of ruthenium are of industrial relevance in extreme ultraviolet (EUV) lithography machines, where they are used as a capping layer on top of EUV multilayer mirrors to prevent oxidation [30–35]. Moreover, thin layers of Ru are also used to enhance the near-IR emissivity of thin membranes, or pellicles, used in EUV lithography machines to protect photomasks. Pellicles can become hot

#438286 https://doi.org/10.1364/OE.438286
Journal © 2021 Received 21 Jul 2021; revised 1 Sep 2021; accepted 10 Sep 2021; published 21 Sep 2021

Optics EXPRESS

and cool typically via emission of thermal radiation [36]. There is thus a significant interest in using photoacoustics to study the material properties of Ru.

In this paper, we show the generation of extremely high-frequency acoustic waves in ruthenium layers deposited on glass. We demonstrate that the optical response of the Ru layers to acoustic waves is mostly governed by the thermo-optic and strain-optic effects. Furthermore, we measure strain waves with frequencies as high as 750 GHz and we show that, for ultra-thin layers, the speed of sound is a strong function of layer thickness. Moreover, we observe that the decay time of the strain-wave-induced oscillations of the diffraction efficiency decreases strongly with decreasing layer thickness and, thus, with increasing strain wave frequency. We attribute this to a layer-thickness (and thus a frequency) dependent acoustic impedance mismatch with the glass substrate which allows for higher transmission of the strain wave into the substrate with a corresponding faster decay of the measured signals. Finally, we demonstrate that for ultra-thin Ru layers, the frequency of the excited strain wave is stable after approximately t = 1.8-2.0 ps. However, if we extrapolate the measured strain-wave-induced diffraction, starting from 1.8-2.0 ps, back to t = 0, when both pump and probe overlap in time on the sample, we find that the extrapolated starting phase equals $-\pi/2$. This seems rather unlikely and therefore suggests that in the first 1.8-2.0 ps, dynamical changes occur in the frequency and/or the phase of the generated strain wave.

2. Experimental setup

In Fig. 1 we show a schematic depiction of the pump-probe setup. The laser system is a 1 kHz repetition rate Ti:Sapphire regenerative amplifier (Astrella, Coherent) which generates laser pulses with a central wavelength of 800 nm, a pulse energy of 6 mJ, and a pulse length of 35 fs. The laser output is split into two by a beam splitter.

The 800 nm beam reflected by the beam splitter acts as the pump beam and first passes through a variable optical delay line. The beam is frequency-doubled to a central wavelength of 400 nm using a 100 μm thick BBO crystal and passes through a mechanical chopper, reducing the repetition rate to 500 Hz. After the chopper, the pump beam passes through a 50/50 beamsplitter, creating two pump beams with equal intensity. Both beams are focused onto the sample to a spot with a diameter of approximately 500 μm. Care is taken to ensure that the two 400 nm pump pulses overlap in both space and time, creating an interference pattern on the sample. In doing so, the Ru layer is excited only in the bright fringes of the interference pattern and remains unperturbed in the dark fringes. As optical excitation modifies the optical properties of the material, this leads to a transient-grating that is capable of diffracting light. The period of the grating is determined by the 400 nm wavelength and the angle between the two beams and has a value of approximately 6 μm [37].

The 800 nm beam transmitted by the beam splitter, which acts as the probe beam, enters an optical parametric amplifier (OPA, HE-TOPAS, LightConversion). This converts the 800 nm pulses into pulses with a wavelength of 1300 nm. After the OPA, the beam is frequency-doubled to generate pulses with a central wavelength of 650 nm. This beam is then focused onto the sample to a spot with a diameter of approximately 250 μm.

The Ru layers are made by plasma-assisted sputter deposition on a chemically cleaned glass substrate. In Fig. 2, we show Atomic Force Microscopy (AFM) images of a 20 nm, 5.0 nm, and 2.3 nm thick Ru layer, deposited on glass. From these images, we find that the root mean square (RMS) surface roughness values are 520 pm, 580 pm, and 460 pm for the 20 nm, 5.0 nm, and 2.3 nm thick layer samples, respectively. We also took an AFM image of the glass substrate (not shown here) and obtained an RMS roughness value of 430 pm. Ellipsometry measurements on a thick 107 nm Ru layer have shown that the Ru layers have a complex refractive index of $\tilde{n} = 3.0 + 5.7i$ and $\tilde{n} = 5.9 + 6.0i$ at 400 nm and 650 nm, respectively. Furthermore, for all Ru layer

Optics EXPRESS

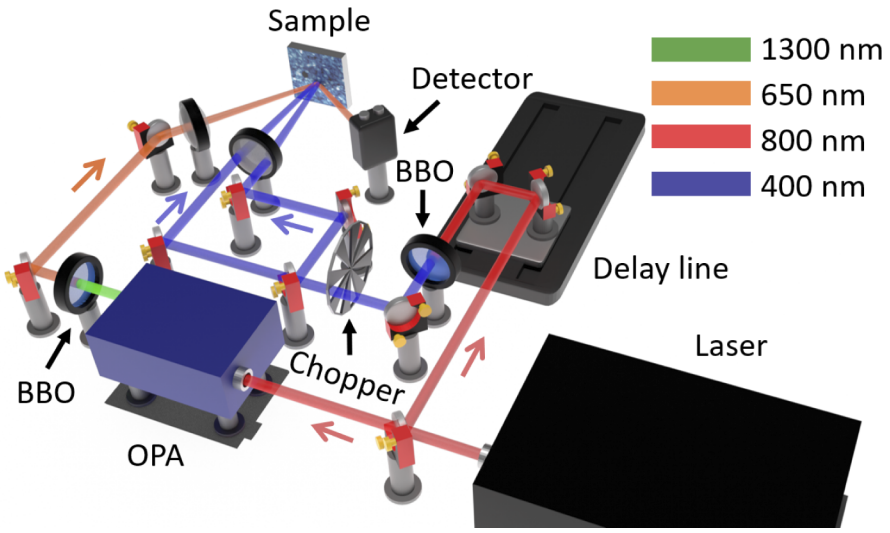

Fig. 1. Schematic drawing of the setup used in our experiments. The output of a 1 kHz repetition rate regenerative amplified Ti:Sapphire laser is split into a pump beam and a probe beam. The pump first travels through an optical delay line after which the optical frequency is doubled using a BBO crystal. Afterward, the pump is optically chopped to reduce the repetition rate by 50%. The pump is split into two beams. These two pump beams overlap in time and, noncollinearly, in space to form an intensity grating on the Ru surface. The probe is sent to an optical parametric amplifier (OPA) set to generate a signal beam with a wavelength of 1300 nm. This beam is subsequently frequency-doubled to create a beam with a central wavelength of 650 nm. Afterward, the probe beam is focused onto the sample in the same spot as the pump pair.

thicknesses we have measured an absolute absorption between 27% and 34% at a wavelength of 400 nm.

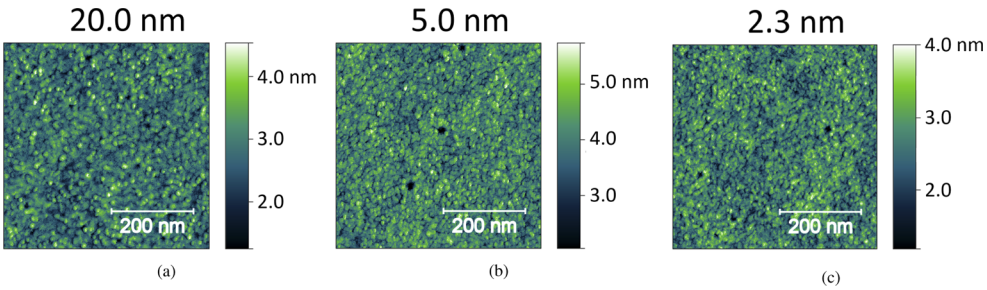

Fig. 2. AFM images of three Ru layers on glass with thicknesses of 20 nm (a), 5.0 nm (b), and 2.3 nm (c). The RMS surface roughness for these thicknesses is 520 pm, 580 pm, and 460 pm, respectively.

3. Results and discussion

In the transient-grating measurements discussed below, the surface area on the sample illuminated by the pump and probe beam was kept constant, for each sample. The pump power was adjusted to values below the damage threshold of each sample. It was found that thinner samples were damaged at lower fluences than thicker samples. Nevertheless, we found that the maximum laser

Optics EXPRESS

fluences deposited on these layers before damage occurs were surprisingly high. For example, on a Ru layer of 5 nm thick, damage only occurred when each of the pump pulses incident with a 500 μm diameter spot had a fluence of 2×10^{-3} J/cm^2. This is most probably related to the high melting point of Ru and the fact that Ru seems to adhere to the surface of the glass very well, in contrast to a material such as gold. The probe beam power was chosen to maximize signal-to-noise, but low enough to ensure that no self-induced probe reflection changes were measured. Although we are primarily interested in thin layers with a thickness of less than 20 nm, we also performed experiments on a relatively thick layer of 107 nm Ru for comparison.

3.1. 107 nm thick Ru

In Fig. 3, we plot the time-dependent normalized diffraction efficiency of a 107 nm Ru layer as a function of time delay between the pump and probe pulses. The solid line going through the data points is a running average over three data points. At t = 0 ps we measure a pulse-length-limited increase in the probe diffraction efficiency. This response is attributed to the quasi-instantaneous heating of the electron gas, creating a grating in the electron temperature [38]. Afterward, the electron gas energy thermally diffuses into the material, while simultaneously cooling by transferring energy to the lattice via electron-phonon coupling [12,39]. This causes the lattice to heat up in the same spatially periodic manner as the incident intensity profile. Consequently, a grating in the lattice temperature is generated, which manifests itself as a background diffraction signal. The lattice energy will thermally diffuse deeper into the material, lowering the temperature near the surface where the probe pulse samples the grating to a depth roughly equal to the probe optical penetration depth of 8.5 nm. This causes the background diffraction to decay within 100-150 ps.

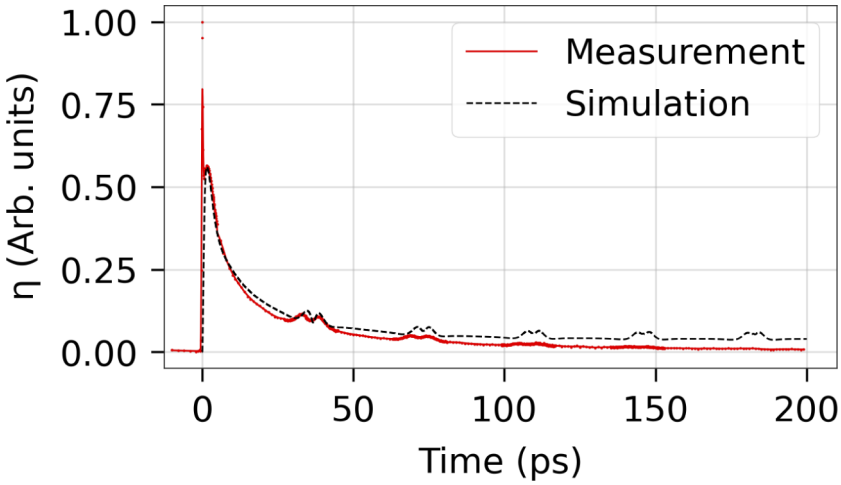

Fig. 3. Transient-grating pump-induced diffraction efficiency of the 650 nm central wavelength probe beam on a 107 nm Ru layer deposited on glass, as a function of time. The black dashed line is a calculation of the diffraction efficiency induced by a combination of the strain- and thermo-optic effect. This calculation does not include damping of the acoustic wave or partial transmission of the wave into the glass substrate.

Superimposed on the background diffraction we measure periodic perturbations in the diffraction efficiency. These perturbations are caused by a strain wave that is launched near the surface due to rapid lattice heating which creates a thermal stress [3,40]. The strain wave travels through the Ru layer, partially reflects off the substrate, and travels back to the Ru/air interface, where it is detected by measuring the probe diffraction. The acoustic echo can induce changes

Optics EXPRESS

in the diffraction efficiency via both the strain-optic effect and by physical displacement of the surface [4,6,7]. From the periodicity of the acoustically induced diffraction changes, we can determine that the speed of sound for our 107 nm thick ruthenium layer is approximately 6030 m/s, which is close to the literature value for the speed of sound in bulk Ru of 5970 m/s [41].

To simulate the strain wave-induced-diffraction, we start with the transient temperature distribution of the Ru layer after excitation with an ultrafast laser pulse. The most widely used model to calculate the temperature dynamics of metals after optical excitation is the two-temperature model (TTM) [42]. In the TTM, energy exchange between the lattice and the electron gas is governed by a set of two coupled differential equations [42],

$$\begin{aligned} C_e(T_e)\frac{\partial T_e}{\partial t} &= \frac{\partial}{\partial z}\left(k_e(T_e,T_l)\frac{\partial T_e}{\partial z}\right) - g(T_e - T_l) + S(z,t), \\ C_l\frac{\partial T_l}{\partial t} &= g(T_e - T_l), \end{aligned} \tag{1}$$

where T_e and T_l are the electron and lattice temperature, respectively, k_e is the electron thermal conductivity, z is the depth inside the sample, g the electron-phonon coupling constant, S the laser source term and C_e and C_l the heat capacities of the electron gas and the lattice, respectively. The temperature dependence of the electron gas heat capacity and the electron gas thermal conductivity are given by $C_e(T_e) = A_e T_e$ and $k_e(T_e, T_l) = k_{e,0} T_e/T_l$, respectively, where A_e is the specific heat constant of the electron gas and $k_{e,0}$ is the electron gas thermal conductivity at room temperature. From this set of differential equations, we see that the electron gas will absorb the energy from the laser, after which the electron gas energy will diffuse deeper into the metal, transferring energy to the lattice, thereby heating the lattice. Rapid heating of the lattice will set up a thermal stress σ_z^{th}, given by [3,43]

$$\sigma_z^{th}(z,t) = -3B\beta\Delta T_l(z,t), \tag{2}$$

where B is the bulk modulus of the metal, β the coefficient of linear expansion and ΔT_l the increase in lattice temperature. In order to calculate the thermal-stress-induced-strain wave inside our Ru layers, we follow the derivation as given by Thomsen et al. [43], where we numerically solve the equations of elasticity in the z-direction,

$$\begin{aligned} s_z(z,t) &= \frac{\partial u(z,t)}{\partial z}, \\ \sigma_z(z,t) &= \sigma_{str} + \sigma_z^{th} = (\lambda + 2\mu)s_z(z,t) - 3B\beta\Delta T_l(z,t), \\ \rho\frac{\partial^2 u(z,t)}{\partial t^2} &= \frac{\partial \sigma_z(z,t)}{\partial z}, \end{aligned} \tag{3}$$

where $s_z(z,t)$ is the strain, σ_z is the total stress, which is the sum of the thermal stress σ_z^{th} and the stress induced by the strain wave σ_{str}, λ and μ are the Lamé parameters, u is the displacement and ρ is the density of the material. The periodicity of the transient-grating of 6 μm is approximately three orders of magnitude larger than the sample thickness. This could, in principle, lead to the generation of shear waves which, for the grating period in our experiment, would have a temporal period much longer than the time scale of our experiment, and can thus be ignored [44]. We numerically solve the differential equations given in Eq. (3) by employing a central difference method.

The lattice temperature increase will also influence the diffraction via a thermally-induced spatial grating in the dielectric function, referred to as the thermo-optic effect. We can calculate how the strain-optic, thermo-optic, and surface displacement effects influence the diffraction

Optics EXPRESS

efficiency with [43,45],

$$\eta_{disp} = |irk_z h_0(t)|^2 \propto \left| k_z \int_0^L s_z(z,t)\, \mathrm{d}z \right|^2, \tag{4}$$

$$\eta_{str} = |\delta r_{str}|^2 \propto \left| k_{str} \int_0^L \exp\left(2ik_z nz - \frac{2z}{d_p}\right) s(z,t)\, \mathrm{d}z \right|^2, \tag{5}$$

$$\eta_{th} = |\delta r_{th}|^2 \propto \left| k_{th} \int_0^L \exp\left(2ik_z nz - \frac{2z}{d_p}\right) \Delta T(z,t)\, \mathrm{d}z \right|^2, \tag{6}$$

$$\eta_{tot} \propto |irk_z h_0(t) + \delta r_{str} + \delta r_{th}|^2, \tag{7}$$

where η_{disp}, η_{str} and η_{th} are the diffraction efficiencies induced by *only* the displacement, strain and thermal effects, respectively. η_{tot} is the total diffraction efficiency from a combination of the effects caused by displacement, strain and a thermal background, r the complex optical reflection coefficient, k_z the z-component of the k-vector of the probe beam, h_0 the strain-induced displacement at the surface, L the layer thickness, δr_{str} and δr_{th} the changes to the complex reflection coefficient caused by the strain and the thermal background, respectively, k_{str} the strain-optic coefficient, n the real part of the refractive index, d_p the penetration depth of the incident probe light, and k_{th} the thermo-optic coefficient. For ruthenium, the strain-optic and thermo-optic coefficients are, to the best of our knowledge, not known and are thus used as fitting parameters in our calculations. In Fig. 4 we show calculations of the displacement-, strain-, and thermally- induced normalized diffraction efficiencies separately, for the 107 nm Ru layer. Note that, according to Eq. (7), we cannot simply add the different components of the diffraction efficiencies themselves to get the total diffraction efficiency.

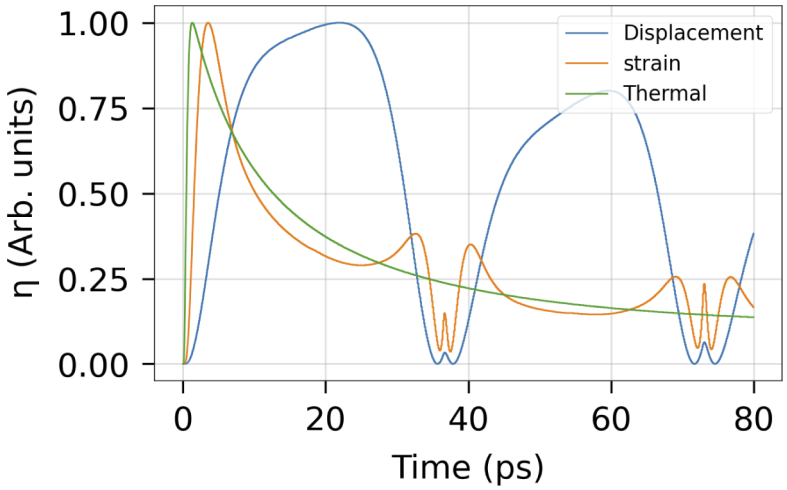

Fig. 4. Calculated diffraction efficiency of *only* the strain-optic, *only* the thermo-optic and *only* the displacement effects. All contributions have been normalized to their respective maximum.

If we compare the shapes of the calculated diffraction curves with the measurement, we see that we find the best resemblance if we take into account only the strain-optic and thermo-optic effects. The dashed curve in Fig. 3 is the calculated diffraction efficiency taking only the strain-optic and thermo-optic effect into account, using the bulk literature values for the Lamé parameters. If we take diffraction induced by surface displacement into account, agreement between the

Optics EXPRESS

measurement and the simulation is not possible. From our simulations, we find the best agreement between the measurement and the calculations when $k_{str}/k_{th} = 4.5 \times 10^4 \times e^{1.5\pi i}$. The phase factor in this fraction represents the difference between the strain-optic and thermo-optic induced optical phase.

3.2. Ultrathin layers

As discussed in the previous section, in the 107 nm thick Ru layer, temporally separated acoustic echoes are measured. When the Ru layer thickness is decreased, it is no longer possible to separate the acoustic echoes in time. This is demonstrated in Fig. 5(a), where we plot the time-dependent diffraction efficiency of two Ru layers with thicknesses of 20 and 5 nm. The total incident pump pulse energy equals 12 μJ and 34 μJ for the 5 nm and 20 nm thick Ru layers, respectively. For both layer thicknesses, we measure a pulse-length-limited increase in diffraction efficiency at t = 0 ps, similar to the measurement performed on the 107 nm Ru sample. However, for the samples shown here, we measure periodic sinusoidal oscillations with a decreasing amplitude on top of a decreasing background. The diffraction efficiency induced by the acoustic waves is on the order of 10^{-9}.

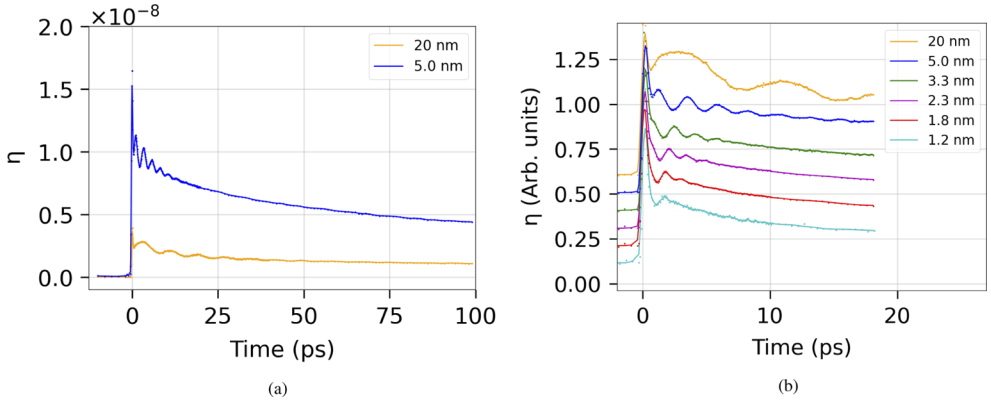

Fig. 5. Transient-grating pump-induced changes to the diffraction efficiency. (a) The measured diffraction efficiency for 20 nm and 5 nm thick Ru layers on a long timescale. (b) The measured diffraction for multiple layer thicknesses, here the curves have been normalized to their respective electronic peaks and have been given an offset for clarity.

When the Ru layer thickness is on the same order as the electron energy diffusion depth the entire layer will heat up homogeneously. Using the two-temperature model, given by Eq. (1), we can calculate that for Ru layers thinner than about 25 nm, the entire layer is homogeneously heated within 4 ps or less. Thus, isotropic stress is formed in the layer, generating a standing acoustic wave, formed by the addition of two counter-propagating acoustic waves. Since the penetration depth of the probe light is approximately 8.5 nm, the probe will also diffract off the acoustic-wave-induced grating at the Ru/glass interface for the ultrathin layers discussed here. The light diffracted off the Ru/glass interface will accumulate an additional optical phase that is determined by the layer thickness and by the phase shift that occurs upon reflection/diffraction off the interface. The difference in optical phase between the beams diffracted off the Ru/glass interface and off the grating at the surface can cause interference between the two diffracted beams and should be considered in future attempts to simulate the measurements.

For the ultra-thin layers, as compared to the 107 nm Ru layer, we would initially expect a constant, thermally induced, background diffraction, since the lattice temperature is equal throughout the entire layer. However, a gradually decreasing background is present. This is attributed to the slow energy diffusion into the underlying glass substrate. We note that this

Optics EXPRESS

is different for the 107 nm thick Ru layer where the relatively slow decay was determined by diffusion of thermal energy deeper into the Ru itself.

The optically generated standing wave results in periodic oscillations in diffraction efficiency after approximately 1 ps. The frequency of such a standing wave is determined by the layer thickness d and the speed of sound of the material v_c and is given by $f = v_c/2d$. If we use the known layer thicknesses and the speed of sound derived from the 107 nm Ru sample, we find that the expected oscillation frequencies are 603 GHz and 150 GHz for the 5 nm and 20 nm thick Ru layer, respectively. However, the measured frequencies of the acoustic oscillations are approximately 420 GHz and 130 GHz for the 5 nm and 20 nm thick layers, respectively.

To investigate the discrepancy between the expected and measured sound frequencies, we performed pump-probe measurements on multiple Ru layer thicknesses, from 1.2 to 20 nm, as shown in Fig. 5(b). Note the shorter timescale when compared to Fig. 5(a). All curves have been normalized to their respective electron diffraction peak at t ≈ 0 ps and have been given a vertical offset for clarity. The figure shows that we measure a general increase in the apparent frequency of the acoustic waves when the layer thickness decreases, as expected. The layer thicknesses have been determined by accurately calibrating the deposition rate of the sputter-coater using a profilometer to measure the thickness of a relatively thick layer of Ru. In addition, after deposition, the layer thicknesses have been experimentally confirmed for the 5.0 and 20 nm thick Ru layer samples using ellipsometry.

To better show only the *acoustic-wave* induced diffraction efficiency, we removed the thermal background by subtracting an exponentially decaying function with a single time constant from the data, see appendix A for more detail. The results are shown in Fig. 6(a). The black dashed line going through each data set represents a fit to the data with a single frequency, exponentially damped sine. In the inset of this figure, we show a zoomed-in version of the 1.8, 2.3, and 3.3 nm measurements. Close inspection of the data shows that the fit slightly deviates from the measured data. The frequency, or the phase, of the measured oscillating acoustic diffraction efficiency changes as a function of time. This was confirmed by repeating the experiment several times.

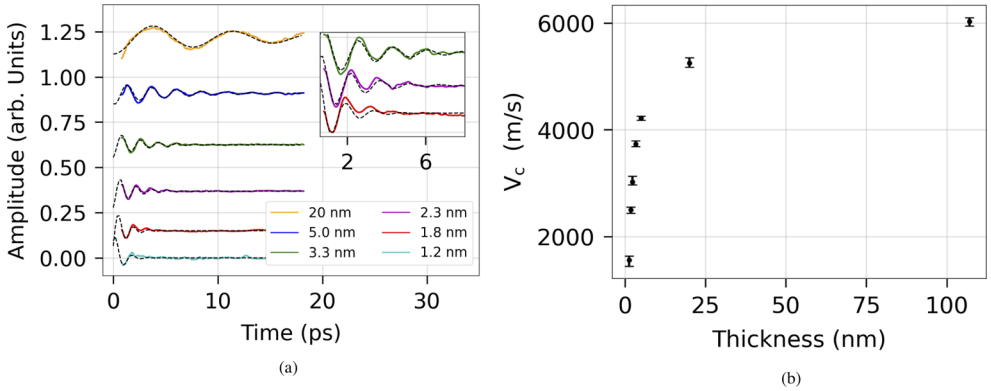

Fig. 6. (a) Measured diffraction efficiency of multiple layer thicknesses, also shown in Fig. 5(b) but with the thermal background removed. The dashed lines correspond to a fit of a single-frequency, damped sine to the data. (b) The speed of sound extracted from the fit as a function of layer thickness.

If we initially ignore this, as the effect seems to be fairly small, and assume a single-frequency acoustic signal, we can extract the frequency from the fit and, combined with the Ru layer thicknesses, we can calculate the effective speed of sound for all Ru layers. This is shown in Fig. 6(b). We find that the effective speed of sound strongly depends on the layer thickness, ranging from 1555 ± 80 m/s for a layer thickness of 1.2 nm to 6030 ± 70 m/s for a layer thickness

Optics EXPRESS

of 107 nm. It has been shown that the sound velocity in thin metal films can decrease as a function of layer thickness due to the thin-film softening effect, which has been reported for thin films of Au [46,47] and Ni [48]. It has also been shown that Young's modulus can decrease with decreasing layer thickness due to changes in crystal structure and grain size [49], which directly influences the speed of sound. Furthermore, although difficult to see in the AFM and SEM measurements, we suspect that the thinnest Ru layers, ≤ 1.8 nm, may not be continuous. This most likely influences the effective speed of sound as well. We caution, however, that Ru can oxidize and form an oxide layer at the surface of ≈ 1 nm thickness. The consequences of these effects on the observed sound velocity and, thus, the sound frequency are difficult to predict.

Another interesting observation is that we measure an increase of the acoustic damping rate for decreasing layer thicknesses, as can be seen in Fig. 7. The red dots show the measured damping rate versus the frequency of the acoustic waves. The blue dot represents the measured damping rate for the frequency corresponding to the 1.2 nm thick Ru layer. Accurate determination of the frequency of the acoustic wave is not possible for the 1.2 nm thick layer because there is only half a period of the oscillation present, as can be seen in Fig. 6(a). However, we do find the strongest damping rate for the frequency corresponding to the 1.2 nm thick layer. The error bars have been determined as the range of frequencies and damping rates for which a reasonable fit to the data, as shown in Fig. 6(a), could be obtained. For the analysis that follows, the blue data point has been excluded due to the relatively high uncertainty in the estimated frequency of the acoustic wave in the 1.2 nm thick layer.

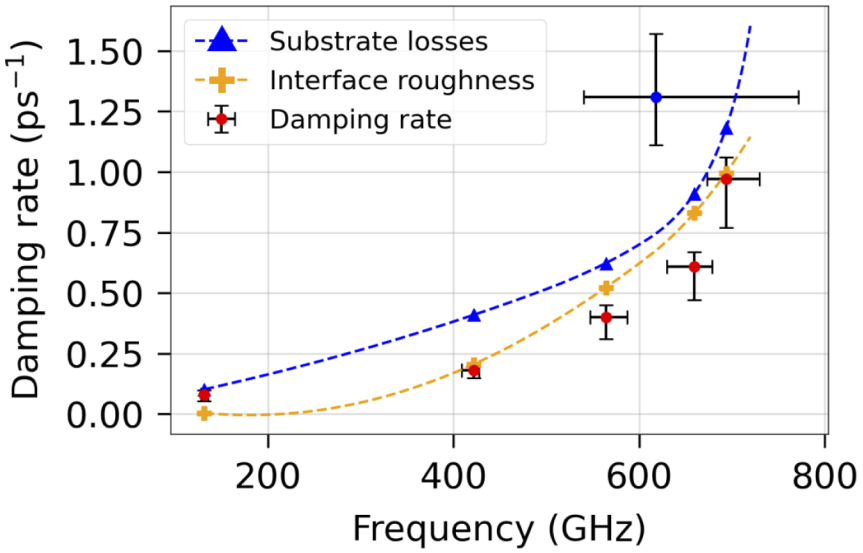

Fig. 7. The red dots show the damping rate versus the frequency of the acoustic wave. The blue dot corresponds to the damping rate acquired for the 1.2 nm thick Ru layer, for which an accurate oscillation frequency could not be determined. The yellow crosses represent the calculated damping rate caused by interface roughness and the dashed line going through the crosses acts as a guide to the eye. The blue triangles represent the calculated damping rate caused by transmission of acoustic energy into the substrate, and again, the dashed line going through the triangles acts as a guide to the eye.

An important mechanism for the observed signal decay in our setup is most likely that sound waves are partially transmitted every time they reach the Ru/glass interface. The transmission and reflection values are determined by the acoustic impedance mismatch between the Ru and the glass. If this mismatch were independent of the frequency, the decay rate would still increase

Optics EXPRESS

for higher frequencies because at higher frequencies, there would be more reflections of the acoustic wave from the Ru/glass interface per unit of time. Another way of phrasing this is to say that the decay time expressed in units of the number of periods of the acoustic wave, would be constant. However, from our measurements we see that the decay is faster for higher frequencies, which may be an indication that the acoustic impedance of the Ru changes as well. This can be understood from the fact that the acoustic impedance of a material is given by $Z = \rho v_c$. Thus, from the measured (see Fig. 6(b)) frequency-dependent speed of sound, we can calculate the frequency-dependent acoustic impedance of the ruthenium. Combined with the acoustic impedance of the glass substrate, $Z_{sub} = 12.5\times10^6$ Ns/m^3 [4], we can calculate the acoustic reflection coefficient for the Ru/glass interface, using

$$R(f) = \left(\frac{Z_{Ru}(f) - Z_{sub}}{Z_{Ru}(f) + Z_{sub}}\right)^2, \tag{8}$$

where $Z_{Ru}(f)$ is the frequency-dependent acoustic impedance of ruthenium. The calculated acoustic impedance at the different measured frequencies can be found in Table 1.

Table 1. Calculated acoustic impedance of Ru at the different measured acoustic frequencies.

Frequency (GHz)	131	421	564	659	693
$\mathbf{Z_{Ru}}$ **(10^6Ns/m^3)**	64.4	52.5	46.4	37.7	31.1

From the acoustic reflection coefficient, we can derive the frequency-dependent decay rate of our measured diffraction signal caused by the loss of acoustic energy into the substrate, which is shown by the blue triangles and the blue dashed line in Fig. 7. We find that the shape of the damping rate caused by substrate losses matches the measured shape of the damping rate reasonably well, despite a quantitative difference in strength. However, we note that the acoustic impedance depends not only on the speed of sound but also on the density. So far, we have used the bulk value for the density of ruthenium in these calculations but, perhaps, the density is different for these thin layers. A more precise calculations would therefore require knowledge of the layer thickness-dependent density of the ruthenium, which we do not have access to. For the present calculation, a fixed ruthenium density has been assumed of 12.45 g/cm^3 [41]. Qualitatively speaking, the agreement of the calculated frequency-dependent damping rate with the measured damping rate would improve if we could assume a higher ruthenium density than the bulk value.

Another mechanism which could contribute to damping of the signal is the surface roughness of the Ru layers. The surface roughness leads to a distribution of the effective thickness across the entire layer. Such a variation in the effective thickness could lead to the generation of a broader spectrum of generated sound frequencies that would give rise to a more strongly damped signal. Note that if the RMS values of the surface roughness are not strongly dependent on layer thickness, the ratio of the RMS roughness value and the layer thickness will determine the relative spread of generated frequencies. Thin layers would thus give rise to a more strongly decaying signal. By taking the height distribution of the ruthenium directly from AFM measurements for each layer thickness, we can calculate the width of frequency distribution of the acoustic wave. From this, we extract the damping rate as a function of the layer thickness, and thus the frequency. The result of this calculation is shown as the orange crosses and the orange dashed line in Fig. 7. We see that the calculated damping due to Ru/Air interface roughness is close to the measured damping rate. However, AFM images show that the glass substrate has a similar surface roughness as the Ru, meaning that the effective thickness could be homogeneous throughout the entire layer if the Ru follows the glass topography. Nevertheless, at this moment we cannot determine whether the topography of the Ru exactly copies that of the glass. This

Optics EXPRESS

means that we cannot state with certainty that the surface roughness could explain the measured rapid damping of the acoustic wave for the thinnest layers.

We note that other decay mechanisms exist as well, such as viscous damping [3,50] which can give a decay which quadratically depends on the frequency. However, our experimental results currently do not allow us to conclude whether interface roughness and/or viscous damping contribute to the measured frequency-dependent damping rate which appears to be dominated by partial transmission of the acoustic wave into the substrate.

3.3. Pump power dependence

In Fig. 8(a) and (b) we show time-resolved pump-probe diffraction measurements on the 5 nm Ru layer and on the 2.3 nm layer, respectively, as a function of the sum of the energies of the two pump pulses. Again, the thermal background has been removed by subtracting a decaying exponential function. The dashed line represents a fit to the data with a single frequency, damped sine. However, rather than fitting to the whole waveform as we have shown in Fig. 6(a), here we start the fit at 2 ps and 1.8 ps for the 5 nm and 2.3 nm layers respectively, indicated by the vertical dashed red lines. The fitted function is then extrapolated back to t = 0 ps. From the fit, we extract acoustic frequencies of 420 ± 10 GHz and 750 ± 15 GHz for the 5.0 nm and 2.3 nm thick layers, respectively. We observe a mismatch between the measured data and the extrapolated sinusoidal fit in approximately the first 2 ps after excitation. This could be due to several reasons. One reason might be that the method used for the subtraction of the thermal background is not perfect. Subtraction of an exponential fit to correct for the slowly decaying lattice temperature during the time that the electron gas cools and still heats the lattice could lead to unreliable results in the first two ps.

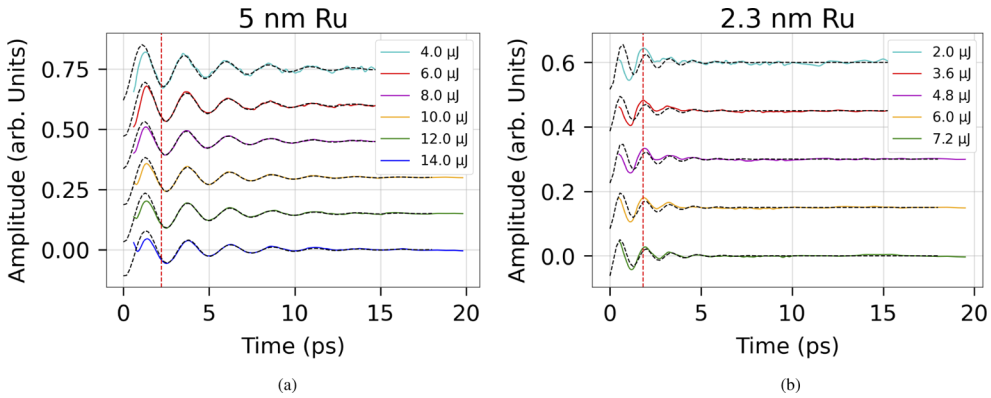

Fig. 8. Measured pump-power dependence of the diffraction for a 5 nm (a) Ru layer and a 2.3 nm (b) Ru layer. The black dashed lines are single frequency dampened sinusoidal fits to the data, starting from the dashed vertical red line and extrapolated backwards to t = 0.

Another reason might be that the frequency of the acoustic wave changes as a function of the lattice temperature. The latter hypothesis is supported somewhat by the fact that TTM calculations show that, under our experimental conditions, the lattice temperature rapidly increases and reaches high values, but stabilizes and remains constant after approximately 2 ps, see Appendix B for more details. However, as we will show later, the frequencies measured after 2 ps when the lattice temperature has stabilized, do *not* depend on the pulse energy and therefore the lattice temperature. This rules out a temperature dependent frequency. After 2 ps the fit matches the data almost perfectly, showing no changes in the frequency of the acoustic wave.

Note that, using the TTM, our calculations show that the lattice temperature in our samples somewhat exceeds the melting point of Ru for the highest pump powers, even when using

Optics EXPRESS

temperature-dependent thermodynamic properties such as the electron-phonon coupling constant and the lattice heat capacity [51]. However, our TTM calculations do not take into account the latent heat of melting, which has been shown to play a key role in high power optical experiments on Ru layers [52]. It has been shown that taking the latent heat of melting into account will keep the (lattice) temperature of the Ru at the melting temperature for a little longer, for pulse energies that are somewhat higher than needed to reach the melting point temperature [52].

In Fig. 9, we show the frequency and phase extracted from the fits, indicating that the frequency and phase, after 2 ps, remain nearly constant. What is surprising here is that for both thicknesses and all pump-powers, the measured starting phase obtained by extrapolating the fit back to t=0 approximately equals $-\pi/2$. This would seem to suggest that at t = 0 there is a non-zero acoustically induced diffraction efficiency. It has been shown that hot electron pressure can also contribute to the generation of stress [53]. Since the stress generated by the hot electron pressure occurs on a somewhat faster timescale than the stress generated by the lattice, the phase of the strain generated by the electron pressure induced stress will be different from the phase of the lattice-heating-induced strain, which changes the phase of the total strain [54].

$$\sigma_e = \gamma_e \Delta E_e, \tag{9}$$

where γ_e is the electronic Grüneisen parameter and ΔE_e is the change in electron gas energy. A similar relationship holds for the lattice temperature-induced stress, which scales linearly with the lattice Grüneisen parameter γ_l. The presence of a significant addition to the strain wave generation by electron pressure has been shown for ultrathin Ni layers [48], where $\gamma_e > \gamma_l$. For ruthenium, however, we have $\gamma_e \approx 0.8$ and $\gamma_l = 2.3$ [55], which means that $\gamma_e < \gamma_l$. Attempts to describe the non-zero starting phase by simulating the layer expansion using a driven harmonic oscillator model [54] where we include electron pressure (not shown here) indicates that its contribution is indeed small and, therefore does not change the phase of the acoustic wave significantly. As electron pressure appears to be an unlikely candidate to explain why the back extrapolated fit has a non-zero value at t = 0, we speculate that during the first 1.8-2.0 ps the phase/frequency of the acoustic wave changes.

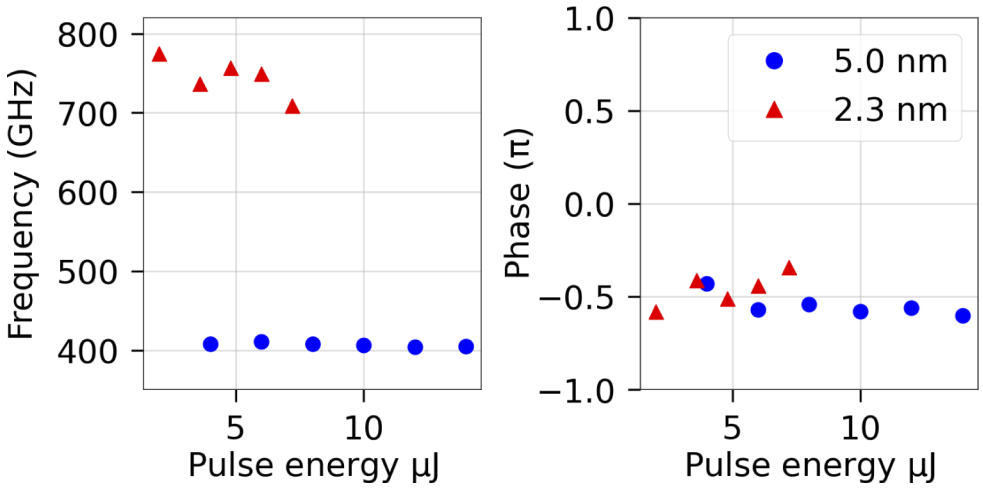

Fig. 9. The starting phase and the frequency of the generated acoustic wave, extracted from the fits shown in Fig. 8(a) and (b). Note that for both thicknesses the frequency and phase remain almost constant as a function of pump pulse energy and that the phase equals -$\pi/2$ for all pump powers.

Optics EXPRESS

4. Conclusion

In this paper, we have shown the ability to generate high-frequency laser-induced acoustic waves in thin Ru layers deposited on glass. We find that for a relatively thick layer of 107 nm Ru, a traveling strain wave is created that perturbs the optical properties periodically and propagates with approximately the bulk speed of sound. Based on our simulations, we find that the acoustically induced optical response of the Ru layer is governed mostly by the thermo- and strain-optic effects. For ultra-thin Ru layers with thicknesses ranging from 1.2 to 20 nm deposited on glass, we demonstrate that we are able to generate extremely high-frequency acoustic waves with frequencies up to 750 GHz. We find that that the speed of sound for these thin layers strongly depends on the layer thickness and thus the frequency of the strain wave. We attribute the layer thickness-dependent speed of sound to possible thin-film softening effects and changes in grain size. Furthermore, this effective frequency-dependent speed of sound results in a frequency-dependent acoustic impedance mismatch between the Ru and the glass substrate, leading to a faster decay of the measured signals with increasing frequency. Moreover, the frequency of the acoustic waves appears to be constant after approximately 2 ps. By back-extrapolation of the signal, we observe an apparent initial phase of $-\pi/2$ for the acoustic-induced optical response. This would suggest that there is a non-zero acoustically induced diffraction efficiency at t = 0. Electron pressure could in principle explain this measured behavior. However, we have calculated that the strain wave generated by the electron pressure in Ru layers is not strong enough to significantly change the phase of the acoustic wave. Therefore, as a non-zero starting phase seems unlikely, we speculate that the phase/frequency of the acoustic wave changes during the first 2 ps after optical excitation.

Appendix A: thermal background removal

For the analysis of the measured acoustic signals from the ultrathin Ru layers, it is important that we separate the acoustic behavior from the slowly decaying thermal background signal. As mentioned in the main body, we attribute the slow thermal decay to lattice heat diffusion into the substrate.

The different steps in the background removal procedure are shown in Fig. 10, where we show the background removal for the 3.3 nm thick Ru layer. First, we take the nearest neighbor average of the data with two neighbors. Visual inspection of the data reveals that there are two decay time scales. First, we observe a rapid decay in the first picosecond, caused by cooling of the electron gas. Afterward, we observe a slow exponential decay up until the end of our signal, attributed to heat diffusion into the substrate. We truncate the measured signal at t = 0.7 ps, indicated by the vertical black dashed line. Truncation of the measured signal is required to largely eliminate the part of the signal caused by the electron dynamics. We have experimented with several truncation times and found that the shortest truncation time where still good agreement between the fit to a single exponentially decaying function and the data is realized, equals t = 0.7 ps. Good agreement between the fit and the data is determined by looking at the overlap between the fit and the data at timescales where the acoustic oscillations have mostly decayed. The function used to fit the background is given by,

$$f(t) = ae^{b(t-c)} + d, \tag{10}$$

where a, b, c, and d are fitting parameters. The exponential fit is shown as the red-dashed line in Fig. 10. After this, the exponential background is subtracted from the data and we are left with the yellow curve, also shown in Fig. 10.

Optics EXPRESS

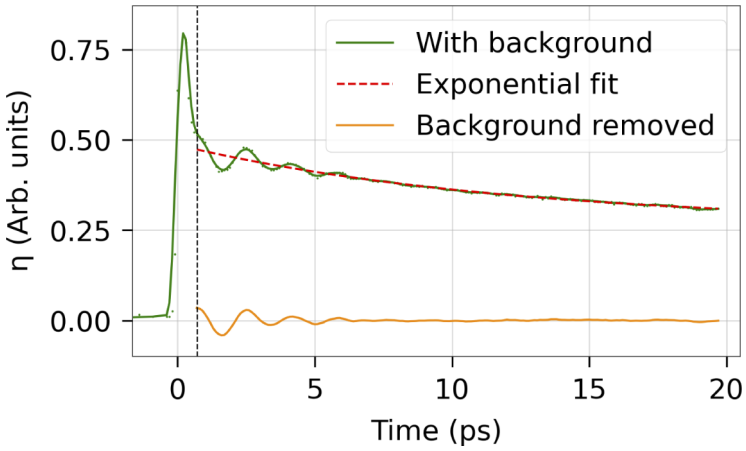

Fig. 10. The different steps undertaken to remove the slowly decaying thermal background from the measured signal on the 3.3 nm thick Ru layer. In green, we show the nearest neighbor average of the normalized acoustic-wave-induced diffracted probe signal as a function of pump-probe delay. The red curve shows the exponential fit to the data truncated at the time t = 0.7 ps, indicated by the vertical dashed line. After subtraction of the exponential fit, we end up with the acoustic signal shown in yellow.

Appendix B: two-temperature calculations

We numerically solve the TTM, according to Eq. (1), to obtain the time-dependent electron and lattice temperature distributions for the Ru layers. The material parameters used in the TTM are shown in Table 2 and the experimental conditions are the same as those described for the experimental results shown in Fig. 8.

Table 2. ruthenium material parameters used in the TTM calculations, taken from Ref. [28].

Parameter	Value
$A_e(\mathrm{Jm^{-3}K^{-2}})$	385
$k_0(\mathrm{Wm^{-1}K^{-1}})$	117
$g(10^{16}\mathrm{Wm^{-3}K^{-1}})$	185
$C_l(10^{6}\mathrm{Jm^{-3}K^{-1}})$	2.95

In Fig. 11(a) and (b) we show the calculated electron and lattice temperature, respectively, as a function of time in the middle of the Ru layer. Due to the small layer thickness and the high thermal conductivity of the Ru, the layer is heated homogeneously. The source term used to simulate heat absorption by the laser in Eq. (1) is calculated using a so-called three-layer model. This model calculates the electric and magnetic field at all locations inside the sample as a function of time, and takes into account all optical interface reflections and their interference. Using the electric and magnetic field we can calculate the absorbed energy per unit volume and per unit time using Poynting's Theorem [56]. Since we excite the sample using a transient-grating geometry, we only deposit energy into the sample in the bright fringes of the grating, whereas no energy is deposited into the dark fringes of the grating. To take this effect into account, the incident total laser energy is multiplied by a factor of two to get the deposited energy inside a bright fringe of the transient grating.

From the TTM calculations we see that immediately after excitation, the electron temperature starts to rise quickly, after which the electron temperature cools down to a constant value within

Optics EXPRESS

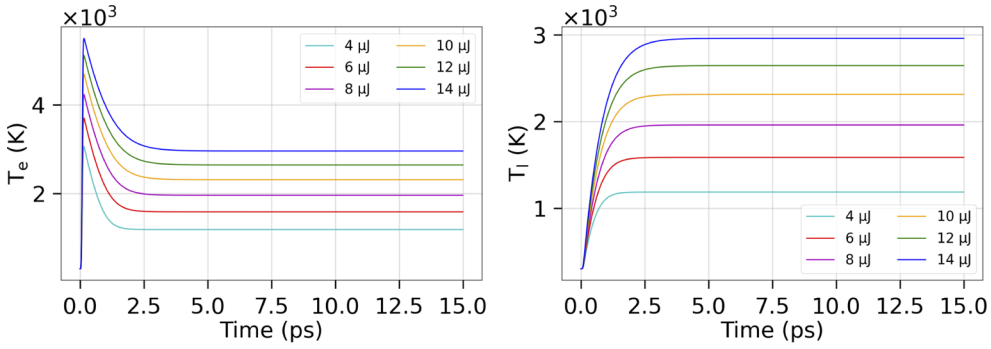

Fig. 11. Electron (a) and lattice (b) temperature as a function of time in the center of a 5 nm thick Ru layer in a bright fringe of the transient grating. The legend shows the total energy of the two incident pump beams which form the transient grating.

2 ps via energy transfer to the lattice. Due to the energy transfer from the electrons to the lattice, the lattice temperature starts to gradually increase. After 2 ps, the lattice temperature has also reached a constant value. It should be noted that for the two highest pump powers, the calculated lattice temperature exceeds the melting temperature of ruthenium, which equals 2583 K [41]. However, our samples did not show any sign of material damage, even after prolonged exposure to the laser pulses. Therefore, we tentatively conclude that the temperature of our Ru layer in the experiments did not exceeded the melting temperature. One explanation for this could be that our TTM calculations do not take the latent heat of melting into account. This will keep the Ru temperature fixed at the melting point temperature for a limited range of increasing pump energies [52]. In addition, there is some uncertainty in the measured excitation and material parameters and, thus, in the final temperatures reached. The TTM calculations for the 2.3 nm thick Ru layer show the same dynamics as those for the 5.0 nm thick Ru layer.

Funding. Nederlandse Organisatie voor Wetenschappelijk Onderzoek; ASML; Universiteit van Amsterdam.

Acknowledgements. The authors would like to thank Dr. Stephen Edward for making the sample which was used as a proof of concept for the measurements performed in this paper. Furthermore, we would like to extend our gratitude to Dr. Igor Milov (University of Twente) for sharing his expertise in fruitful discussions on the thermodynamical properties of ruthenium.

Disclosures. The authors declare no conflict of interest.

Data availability. Data underlying the results presented in this paper are not publicly available at this time but may be obtained from the authors upon reasonable request.

References

1. J. Wang and C. Guo, "Effect of electron heating on femtosecond laser-induced coherent acoustic phonons in noble metals," Phys. Rev. B **75**(18), 184304 (2007).
2. P. Ruello and V. E. Gusev, "Physical mechanisms of coherent acoustic phonons generation by ultrafast laser action," Ultrasonics **56**, 21–35 (2015).
3. H. Zhang, A. Antoncecchi, S. Edward, I. Setija, P. Planken, and S. Witte, "Unravelling phononic, opto-acoustic and mechanical properties of metals with light-driven hypersound," Phys. Rev. Appl. **10**, 1–12 (2020).
4. S. Edward, H. Zhang, I. Setija, V. Verrina, A. Antoncecchi, S. Witte, and P. C. M. Planken, "Detection of Hidden Gratings through Multilayer Nanostructures Using Light and Sound," Phys. Rev. Appl. **14**(1), 014015 (2020).
5. S. Edward, H. Zhang, S. Witte, and P. C. M. Planken, "Laser-induced ultrasonics for detection of low-amplitude grating through metal layers with finite roughness," Opt. Express **28**(16), 23374 (2020).
6. V. Verrina, S. Edward, H. Zhang, S. Witte, and P. C. M. Planken, "Photoacoustic detection of low duty cycle gratings through optically opaque layers," Appl. Phys. Lett. **117**(5), 051104 (2020).
7. V. Verrina, S. Edward, H. Zhang, A. Antoncecchi, S. Witte, and P. C. M. Planken, "Role of scattering by surface roughness in the photoacoustic detection of hidden micro-structures," Appl. Opt. **59**(30), 9499 (2020).

Optics EXPRESS

8. A. Antoncecchi, H. Zhang, S. Edward, V. Verrina, P. C. M. Planken, and S. Witte, "High-resolution microscopy through optically opaque media using ultrafast photoacoustics," Opt. Express **28**(23), 33937 (2020).
9. B. C. Daly, N. C. Holme, T. Buma, C. Branciard, T. B. Norris, D. M. Tennant, J. A. Taylor, J. E. Bower, and S. Pau, "Imaging nanostructures with coherent phonon pulses," Appl. Phys. Lett. **84**(25), 5180–5182 (2004).
10. T. Saito, O. Matsuda, and O. B. Wright, "Picosecond acoustic phonon pulse generation in nickel and chromium," Phys. Rev. B **67**(20), 205421 (2003).
11. J. L. Arlein, S. E. Palaich, B. C. Daly, P. Subramonium, and G. A. Antonelli, "Optical pump-probe measurements of sound velocity and thermal conductivity of hydrogenated amorphous carbon films," J. Appl. Phys. **104**(3), 033508 (2008).
12. G. Tas and H. J. Maris, "Electron diffusion in metals studied by picosecond ultrasonics," Phys. Rev. B **49**(21), 15046–15054 (1994).
13. V. E. Gusev and O. B. Wright, "Ultrafast nonequilibrium dynamics of electrons in metals," Phys. Rev. B **57**(5), 2878–2888 (1998).
14. O. B. Wright and K. Kawashima, "Coherent phonon detection from ultrafast surface vibrations," Phys. Rev. Lett. **69**(11), 1668–1671 (1992).
15. A. Devos and C. Lerouge, "Evidence of laser-wavelength effect in picosecond ultrasonics: Possible connection with interband transitions," Phys. Rev. Lett. **86**(12), 2669–2672 (2001).
16. A. Devos, R. Cote, G. Caruyer, and A. Lefvre, "A different way of performing picosecond ultrasonic measurements in thin transparent films based on laser-wavelength effects," Appl. Phys. Lett. **86**(21), 211903 (2005).
17. D. Schneider, T. Witke, T. Schwarz, B. Schoneich, and B. Schultrich, "Testing ultra-thin films by laser-acoustics," Surf. Coat. Technol. **126**(2-3), 136–141 (2000).
18. H. T. Grahn, H. J. Maris, and J. Tauc, "Time-resolved study of vibrations of a-Ge:H/a-Si:H multilayers," Phys. Rev. B **38**(9), 6066–6074 (1988).
19. B. Perrin, B. Bonello, J. C. Jeannet, and E. Romatet, "Picosecond ultrasonics study of metallic multilayers," Phys. B **219-220**, 681–683 (1996).
20. A. Devos and A. Le Louarn, "Strong effect of interband transitions in the picosecond ultrasonics response of metallic thin films," Phys. Rev. B **68**(4), 045405 (2003).
21. A. Devos and R. Cote, "Strong oscillations detected by picosecond ultrasonics in silicon: Evidence for an electronic-structure effect," Phys. Rev. B **70**(12), 125208 (2004).
22. R. I. Tobey, E. H. Gershgoren, M. E. Siemens, M. M. Murnane, H. C. Kapteyn, T. Feurer, and K. A. Nelson, "Nanoscale photothermal and photoacoustic transients probed with extreme ultraviolet radiation," Appl. Phys. Lett. **85**(4), 564–566 (2004).
23. R. I. Tobey, M. E. Siemens, M. M. Murnane, H. C. Kapteyn, D. H. Torchinsky, and K. A. Nelson, "Transient grating measurement of surface acoustic waves in thin metal films with extreme ultraviolet radiation," Appl. Phys. Lett. **89**(9), 091108 (2006).
24. G. A. Antonelli, P. Zannitto, and H. J. Maris, "New method for the generation of surface acoustic waves of high frequency," Phys. B **316-317**, 377–379 (2002).
25. T. Saito, O. Matsuda, M. Tomoda, and O. B. Wright, "Imaging gigahertz surface acoustic waves through the photoelastic effect," J. Opt. Soc. Am. B **27**(12), 2632 (2010).
26. M. R. Armstrong, E. J. Reed, K. Y. Kim, J. H. Glownia, W. M. Howard, E. L. Piner, and J. C. Roberts, "Observation of terahertz radiation coherently generated by acoustic waves," Nat. Phys. **5**(4), 285–288 (2009).
27. R. M. Slayton, K. A. Nelson, and A. A. Maznev, "Transient grating measurements of film thickness in multilayer metal films," J. Appl. Phys. **90**(9), 4392–4402 (2001).
28. J. P. Colombier, F. Garrelie, N. Faure, S. Reynaud, M. Bounhalli, E. Audouard, R. Stoian, and F. Pigeon, "Effects of electron-phonon coupling and electron diffusion on ripples growth on ultrafast-laser-irradiated metals," J. Appl. Phys. **111**(2), 024902 (2012).
29. M. Bonn, D. N. Denzler, S. Funk, M. Wolf, S. S. Wellershoff, and J. Hohlfeld, "Ultrafast electron dynamics at metal surfaces: Competition between electron-phonon coupling and hot-electron transport," Phys. Rev. B **61**(2), 1101–1105 (2000).
30. I. Nedelcu, R. W. Van De Kruijs, A. E. Yakshin, and F. Bijkerk, "Temperature-dependent nanocrystal formation in Mo Si multilayers," Phys. Rev. B **76**(24), 245404 (2007).
31. A. Haase, V. Soltwisch, F. Scholze, and S. Braun, "Characterization of Mo/Si mirror interface roughness for different Mo layer thickness using resonant diffuse EUV scattering," Proc. SPIE **9628**, 962804 (2015).
32. J. Hrbek, D. G. van Campen, and I. J. Malik, "The early stages of ruthenium oxidation," J. Vac. Sci. Technol., A **13**(3), 1409–1412 (1995).
33. H. Takase, S. Terashima, Y. Gomei, M. Tanabe, Y. Watanabe, T. Aoki, K. Murakami, S. Matsunari, M. Niibe, and Y. Kakutani, "Study of ruthenium-capped multilayer mirror for EUV irradiation durability," Emerg. Lithogr. Technol. **6151**, 615135 (2006).
34. S. Bajt, H. N. Chapman, N. Nguyen, J. Alameda, J. C. Robinson, M. Malinowski, E. Gullikson, A. Aquila, C. Tarrio, and S. Grantham, "Design and performance of capping layers for extreme-ultraviolet multilayer mirrors," Appl. Opt. **42**(28), 5750 (2003).

Optics EXPRESS

35. S. Bajt, Z. R. Dai, E. J. Nelson, M. A. Wall, J. Alameda, N. Nguyen, S. Baker, J. C. Robinson, J. S. Taylor, M. Clift, A. Aquila, E. M. Gullikson, and N. V. G. Edwards, "Oxidation resistance of Ru-capped EUV multilayers," Emerg. Lithogr. Technol. IX **5751**, 118 (2005).
36. P. J. van Zwol, D. F. Vles, W. P. Voorthuijzen, M. Péter, H. Vermeulen, W. J. van der Zande, J. M. Sturm, R. W. van de Kruijs, and F. Bijkerk, "Emissivity of freestanding membranes with thin metal coatings," J. Appl. Phys. **118**(21), 213107 (2015).
37. H. J. Eichler, P. Günter, and D. W. Pohl, *Laser-Induced Dynamic Gratings*, vol. 50 *of Springer Series in Optical Sciences* (Springer Berlin Heidelberg, Berlin, Heidelberg, 1986).
38. S. Edward, A. Antoncecchi, H. Zhang, H. Sielcken, S. Witte, and P. C. M. Planken, "Detection of periodic structures through opaque metal layers by optical measurements of ultrafast electron dynamics," Opt. Express **26**(18), 23380–23396 (2018).
39. C.-K. Sun, F. Vallée, L. H. Acioli, E. P. Ippen, and J. G. Fujimoto, "Femtosecond-tunable measurement of electron thermalization in gold," Phys. Rev. B **50**(20), 15337–15348 (1994).
40. O. Matsuda, M. C. Larciprete, R. Li Voti, and O. B. Wright, "Fundamentals of picosecond laser ultrasonics," Ultrasonics **56**, 3–20 (2015).
41. G. Samsonov, *Handbook of the physicochemical properties of the elements* (IFI-Plenum, New York - Washington, 1968).
42. S. I. Anisimov, B. L. Kapeliovich, and T. L. Perel'man, "Electron emission from metal surfaces exposed to ultrashort laser pulses," J. Exp. Theor. Phys. **39**, 375–377 (1974).
43. C. Thomsen, H. T. Grahn, H. J. Maris, and J. Tauc, "Surface generation and detection of phonons by picosecond light pulses," Phys. Rev. B **34**(6), 4129–4138 (1986).
44. G. de Haan, V. Verrina, A. J. L. Adam, H. Zhang, and P. C. M. Planken, "Plasmonic enhancement of photoacoustic-induced reflection changes," Appl. Opt. **60**(24), 7304–7313 (2021).
45. T. F. Crimmins, A. A. Maznev, and K. A. Nelson, "Transient grating measurements of picosecond acoustic pulses in metal films," Appl. Phys. Lett. **74**(9), 1344–1346 (1999).
46. K. Uozumi, T. Nakada, and A. Kinbara, "Sound velocity and internal friction in vacuum deposited gold films," Thin Solid Films **12**(1), 67–70 (1972).
47. P. J. Wang, C. C. Shen, K. Y. Chou, M. H. Ho, J. K. Sheu, and C. K. Sun, "Studying time-dependent contribution of hot-electron versus lattice-induced thermal-expansion response in ultra-Thin Au-nanofilms," Appl. Phys. Lett. **117**(15), 154101 (2020).
48. K. Y. Chou, C. L. Wu, C. C. Shen, J. K. Sheu, and C. K. Sun, "Terahertz Photoacoustic Generation Using Ultrathin Nickel Nanofilms," J. Phys. Chem. C **125**(5), 3134–3142 (2021).
49. C. Birleanu, M. Pustan, V. Merie, R. Müller, R. Voicu, A. Baracu, and S. Craciun, "Temperature effect on the mechanical properties of gold nano films with different thickness," IOP Conf. Ser. Mater. Sci. Eng. **147**, 012021 (2016).
50. H. Zhang, A. Antoncecchi, S. Edward, P. Planken, and S. Witte, "Ultrafast laser-induced guided elastic waves in a freestanding aluminum membrane," Phys. Rev. B **103**(6), 064303 (2021).
51. N. Medvedev and I. Milov, "Electron-phonon coupling in metals at high electronic temperatures," Phys. Rev. B **102**(6), 064302 (2020).
52. I. Milov, I. A. Makhotkin, R. Sobierajski, N. Medvedev, V. Lipp, J. Chalupský, J. M. Sturm, K. Tiedtke, G. de Vries, M. Störmer, F. Siewert, R. van de Kruijs, E. Louis, I. Jacyna, M. Jurek, L. Juha, V. Hájková, V. Vozda, T. Burian, K. Saksl, B. Faatz, B. Keitel, E. Plönjes, S. Schreiber, S. Toleikis, R. Loch, M. Hermann, S. Strobel, H.-K. Nienhuys, G. Gwalt, T. Mey, H. Enkisch, and F. Bijkerk, "Mechanism of single-shot damage of Ru thin films irradiated by femtosecond extreme UV free-electron laser," Opt. Express **26**(15), 19665 (2018).
53. V. E. Gusev, "On the duration of acoustic pulses excited by subpicosecond laser action on metals," Opt. Commun. **94**(1-3), 76–78 (1992).
54. M. Perner, S. Gresillon, J. März, G. Von Plessen, J. Feldmann, J. Porstendorfer, K. J. Berg, and G. Berg, "Observation of hot-electron pressure in the vibration dynamics of metal nanoparticles," Phys. Rev. Lett. **85**(4), 792–795 (2000).
55. Y. Petrov, K. Migdal, N. Inogamov, V. Khokhlov, D. Ilnitsky, I. Milov, N. Medvedev, V. Lipp, and V. Zhakhovsky, "Ruthenium under ultrafast laser excitation: Model and dataset for equation of state, conductivity, and electron-ion coupling," Data Br. **28**, 104980 (2020).
56. J. H. Poynting, "On the transfer of energy in the electromagnetic field," Philos. Trans. R. Soc. London **175**, 343–361 (1884).